

# Large Eddy Simulation of a Turbulent Wake behind a Body of Revolution at $Re_D = 5000$

Fengrui Zhang\* and Yulia Peet†

*School for Engineering of Matter, Transport and Energy, Arizona State University*

This study is concerned with the numerical investigation of a three-dimensional wake behind a body of revolution via Large-eddy Simulations. Large-eddy Simulations with the Reynolds number  $Re_D = 5000$  based on the bluff body diameter is performed using a high-order spectral-element solver Nek5000. The focus of the study is on characterizing the wake asymmetries and time-dependent behavior observed in previous experimental studies with similar bluff body models. The time-dependent history of the wake meandering and rotating behavior will be presented.

## I. Introduction

Turbulent wakes behind bluff bodies represent a canonical case of interest in the study of turbulence, and are also relevant in a variety of engineering applications, including transport industry and naval operations, to name a few. While planar wakes, such as wakes produced by circular cylinders, flat plates and airfoils, have been rather extensively investigated, a significantly less attention has been paid to the structure and physics of the three-dimensional wakes, e.g., produced by the bodies of revolution, in spite of their importance in realistic applications. A few (predominantly experimental) studies of three-dimensional wakes behind the bodies of revolution that do exist, however, point to very interesting and rich physics behind these flows [1–6]. One of the intriguing facts documented by the experimental observations of bluff body wakes is the apparent flow asymmetry, even though the body model itself is perfectly axisymmetric [1, 4]. The 3D turbulent wake flow seems to be a highly unstable system, with even minute perturbations to the axisymmetric conditions (pitch angle, model support) causing large asymmetries, beyond the ones expected from the magnitude of the perturbations themselves [2, 3]. Another interesting phenomenon observed in 3D wakes is a low-frequency dynamics associated with the azimuthal wake meandering occurring on very slow time scales [4–6]. The two phenomenon are likely not unrelated.

The focus of the present study is to investigate the mechanisms associated with the wake meandering and rotation behind three-dimensional bluff bodies, and a potential implication of the unsteady behavior on the observed flow asymmetries documented in experiments. We numerically reproduce the experiments of Gentile et al. [6] who studied the near wake (from  $x = 0.375D$  to  $x = 1.5D$ ) behind a spherically blunted tangent ogive cylinder, albeit at a lower Reynolds number ( $Re_D = 5 \times 10^3$ ) vs. the experimental  $Re_D = 6.7 \times 10^4$ . We also do not include the model support in the simulations. Nonetheless, a qualitative comparison of the major findings presented in the experimental study related to the time-dependent dynamics of the backflow meandering is possible. We would like to note that there are not many documented high-fidelity simulations of the turbulent wake behind a body of the revolution, although several recent computational studies of the wakes past a sphere can be mentioned in this respect [7–9].

## II. Numerical Method

The current study is performed with the spectral-element code Nek5000 which is an open source high-order solver [10]. It employs a spectral element numerical method (SEM) that combines the geometric flexibility of finite elements with the spectral convergence of global spectral methods [11, 12]. SEM is based on a weak formulation of governing equations. Solution to the weak formulation of the Navier-Stokes equations is sought for the velocity, temperature and pressure represented in the polynomials spaces  $X^N$  and  $Y^N$ , which are finite-dimensional subsets of  $\mathcal{H}_0^1(\Omega)$  and  $L^2(\Omega)$ , respectively,  $\Omega$  is the computational domain [12, 13]. For example, for velocity in an element  $\Omega^e$ , we have the approximation  $\mathbf{u}(\mathbf{x})|_{\Omega^e} = \sum_{i,j,k=1}^N \mathbf{u}_{ijk}^e h_i(r) h_j(s) h_k(\zeta)$ , where the basis functions  $h_i(r)$ ,  $i = 0, \dots, N$ , are Lagrange interpolating polynomials defined on Gauss-Legendre-Lobatto quadrature points,  $\xi_j$ , such that  $h_i(\xi_j) = \delta_{ij}$  [12]. A general motivation for the use of high-order methods is in their superior accuracy without sacrificing efficiency [14].

\*Ph.D. student, AIAA member, e-mail: fzhang82@asu.edu

†Assistant Professor, AIAA member, e-mail: ypeet@asu.edu

Nek5000 is also known for its extreme scalability [15–19]. The incompressible version of the code is used in the current simulations. A high-order modal filtering [20, 21] with a filter strength of 0.1 is employed as an SGS model in the Large Eddy Simulations.

### III. Model set-up and boundary conditions

The current simulations employ a rigid body model of an ogive cylinder with a spherically blunted leading edge shown in Figure 1, whose geometry coincides with the one in experiments of Gentile et al [6]. A computational domain is cylindrical, with a view of a streamwise-radial slice shown in Figure 2. The hexahedral numerical mesh required for Nek5000 calculations was constructed using Ansys Icem, output into the exo format, and converted to the format that can be read by Nek5000 using the open-source exo2nek converter available with Nek5000 version 17 distribution. During the mesh generation procedure, the mesh constructed by Ansys Icem is enhanced from Hex8 to Hex27 element configuration. A partial view of the computational mesh utilized in this study can be seen in Figure 3, where only element boundaries are shown.

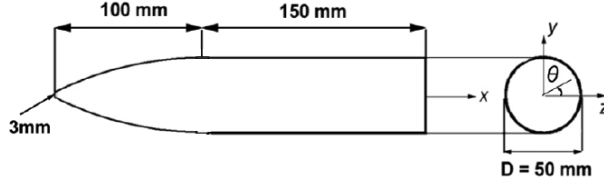


**Fig. 1 Sketch of the ogive-cylinder [6].**

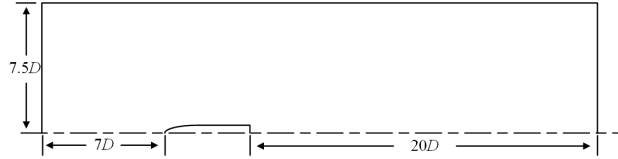
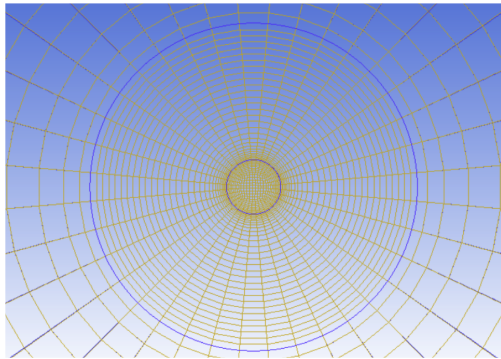
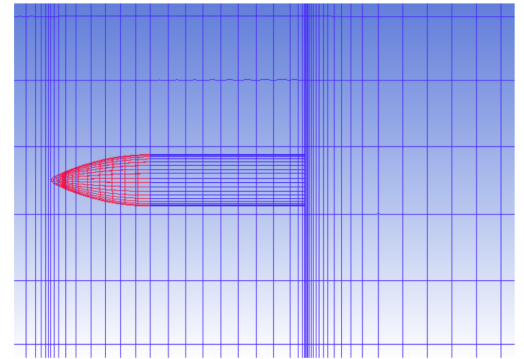


**Fig. 2 Streamwise-radial view of the computational domain.**

The current simulations employ 5th order tensor-product polynomials in each coordinate direction resulting in a  $6^3$  nodal stencil within each element. The element count and the corresponding nodal count (based on Gauss-Legendre Lobatto nodes) is 142,200 and 30.672 mln., respectively. The mesh details in wall units are shown in Table 1.



(a) Spanwise-vertical cross-sectional view showing the O-mesh around the cylindrical bluff body and the mesh in the wake behind the body



(b) Streamwise-vertical cross-sectional view

**Fig. 3 A view of the numerical mesh. Only element boundaries are shown.**

**Table 1** Mesh details.  $x$ ,  $r$ , and  $s$  represent streamwise ( $x$ ), radial ( $r$ ), and azimuthal ( $s$ ) directions. Plus units are based on  $u_\tau$  computed as a temporally and a surface-averaged skin friction velocity for the ogive cylinder body. Minimum and maximum values are based on the minimum and maximum distances between the GLL points across all the elements in a particular direction.

$\Delta x_{min}^+$	$\Delta x_{max}^+$	$\Delta r_w^+$	$\Delta r_{max}^+$	$\Delta s_{min}^+$	$\Delta s_{max}^+$
0.54	12.94	0.43	3.06	2.38	14.12

Boundary conditions at the rigid model surface are no-slip, while the uniform unperturbed free-stream of velocity  $U_\infty$  parallel to the model axis of rotation (no pitch or yaw) is supplied at the inflow, and the stabilized boundary conditions [22] are used at the outflow. The axis aligned with the free-stream (streamwise) direction is denoted as  $x$  axis, while a vertical-spanwise cross-sectional plane contains  $y$  and  $z$  axes. Zero-stress boundary conditions are used at the outer boundaries of the domain. All variables are normalized with the characteristic length scale  $D$  (cylinder diameter), and the characteristic velocity  $U_\infty$ . The time step in the current simulations corresponds to  $\Delta T = 2.5 \times 10^{-5}$  s in dimensional units (seconds), which can be related to a non-dimensional value of  $\Delta T^* = \Delta T U_\infty / D = 5 \times 10^{-4}$ .

#### IV. Results

A snapshot of the instantaneous streamwise velocity in the wake of the bluff body is shown in Figure 4. A region of the low momentum flow immediately behind the abrupt trailing edge of the body corresponding to a flow separation extends by approximately  $1.85D$  in a streamwise direction. The streamwise extent of the separation zone is longer than the one observed in experiment. The reason could be that the upstream boundary layer around the body is not tripped in the simulation.

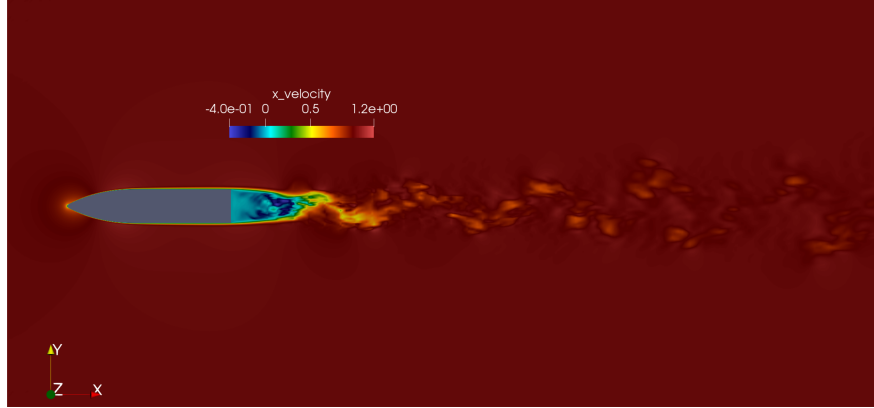


**Fig. 4** Instantaneous snapshot of a wake behind bluff body. Streamwise velocity is shown.

A backflow centroid (barycenter) can be calculated at each cross-stream ( $y$ - $z$ ) cross-section based on momentum-deficit [6, 23]

$$\bar{y}_c(x, t) = \frac{\int \int (u_\infty - u(x, y, z, t)) y d z d y}{\int \int (u_\infty - u(x, y, z, t)) d z d y}, \quad (1)$$

$$\bar{z}_c(x, t) = \frac{\int \int (u_\infty - u(x, y, z, t)) z d z d y}{\int \int (u_\infty - u(x, y, z, t)) d z d y} \quad (2)$$

or based on pressure [4]

$$\bar{y}_c(x, t) = \frac{\int \int p(x, y, z, t) y d z d y}{\int \int p(x, y, z, t) d z d y}, \quad (3)$$

$$\bar{z}_c(x, t) = \frac{\int \int p(x, y, z, t) z d z d y}{\int \int p(x, y, z, t) d z d y} \quad (4)$$

and serves as a convenient measure to judge the wake asymmetry and time-dependent characteristics. Instantaneous and temporally-filtered snapshots of streamwise velocity at  $x = 1.125D$  superimposed by barycenters for different time steps showing the motion of the wake structure are presented in Figure 5. In both instantaneous and temporally-filtered figures, the low-speed area (dark blue) concentrates on the left half of the domain at  $T^* = 32$ , which is consistent with the location of the momentum-deficit-based barycenter. However, at  $T^* = 64$ , the low-speed area splits up and it is hard to identify the flow structure from the instantaneous result. In the temporally-filtered figure, we can see that the low-speed area is rotated between  $T^* = 32$  and  $T^* = 64$ . We should note that the pressure-based barycenter locates so close to the geometric center that these two spots almost coincide in the figure.

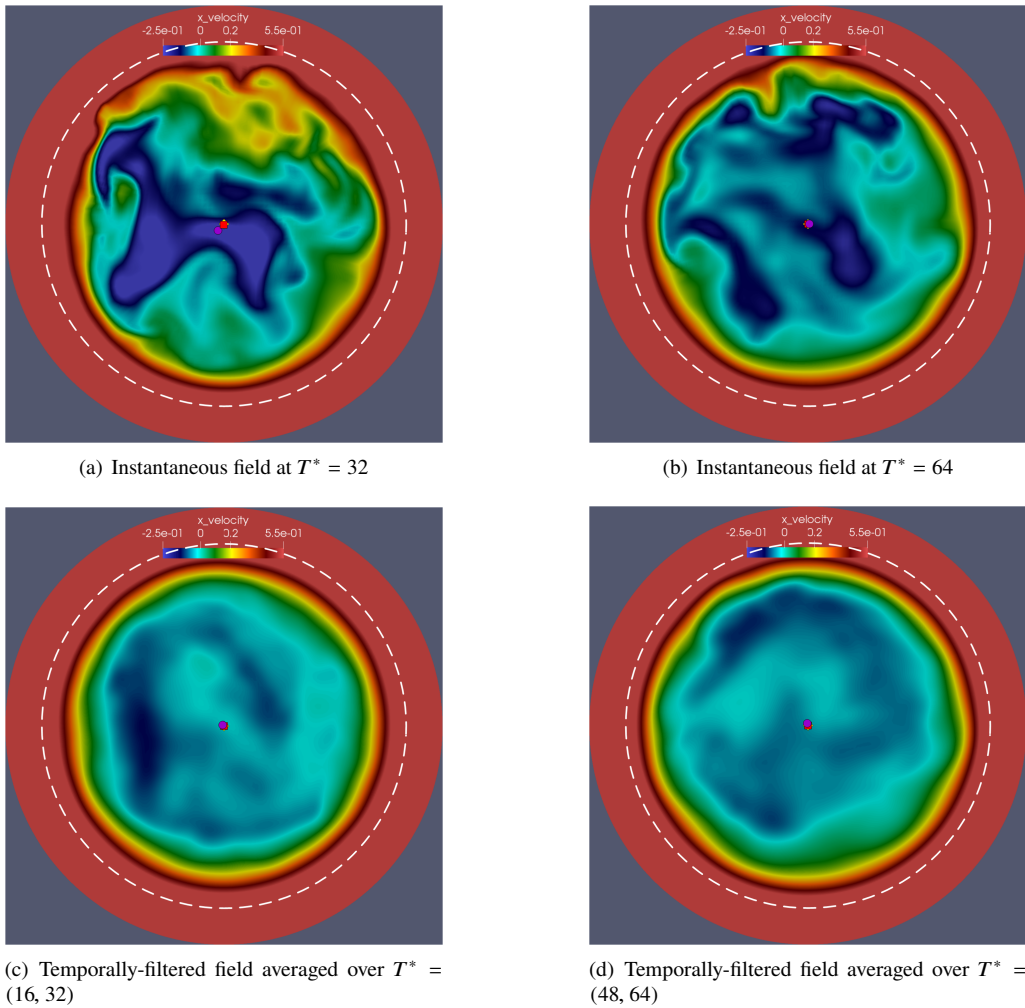


**Fig. 5 Instantaneous and temporally-filtered wake structure (averaged over a non-dimensional time of  $T^* = 16$ ) at  $x = 1.125 D$ . The yellow diamond is the geometric center. The purple circle is the momentum-deficit-based barycenter. The red square is the pressure-based barycenter. The dash curve represents the edge of the cylinder.**

A probability distribution of the momentum-deficit-based barycenter position in the azimuthal plane at different streamwise distances behind the trailing edge is presented in Figure 6 collected over the non-dimensional simulation

time  $T^* = 96$ , and the pressure-based barycenter in Figure 7. Apparent wake asymmetries are noted for both barycenter measures. In the near-wake region, the wake misalignment grows as the wake moves downstream, on the contrary, in the experiment [6] from the results at  $x = 0.375D$  and  $x = 1.125D$  we see that the barycenter spread shrinks. This difference could be the result of the different boundary layer state on the body surface. In the far-wake region ( $x = 9.0D$ ), the momentum-deficit-based barycenter moves farther away from the geometric centroid, while for the pressure-based barycenter, however, the spread is more compact towards the geometric center. Note that the axis range of the pressure-based barycenter figure is scaled to have a clear spread. The comparison of the distributions of these two barycenter measures is shown in Figure 8. It is in line with the observation from Figure 5 that the pressure-based barycenter locates closer to the center-line.

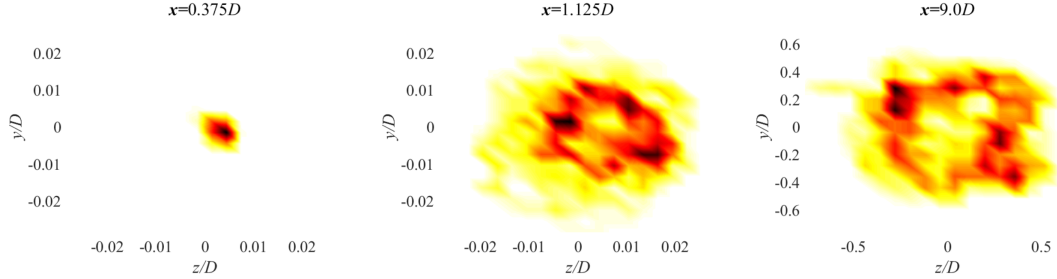


**Fig. 6 Probability distribution of the momentum-deficit-based centroid locations collected over a non-dimensional simulation time of  $T^* = 96$ . Dark red corresponds to a high number of occurrences, and light yellow - to a low number. Note the change in the axis limits for  $x = 9.0 D$ .**

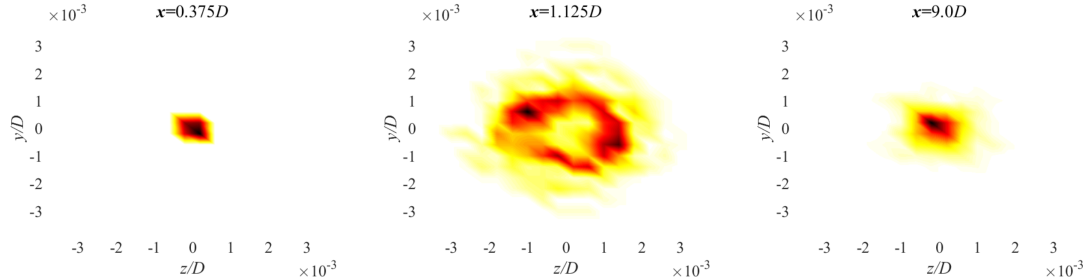


**Fig. 7 Probability distribution of the pressure-based centroid locations collected over a non-dimensional simulation time of  $T^* = 96$ . Dark red corresponds to a high number of occurrences, and light yellow - to a low number. Note the change in the axis limits compared to Figure 6.**

Since the upstream boundary layer is not tripped in the simulations, as opposed to experiments, the boundary layer remains laminar throughout the body surface, and the vortex shedding does not occur right at the trailing edge. Instead, the wake develops for about  $1.5D$  downstream and then begins to oscillate. Three probes are set on the streamwise-vertical plane of symmetry in the wake to capture the vortex shedding motion, see Figure 9. The FFT results of the pressure signal at all three probes show a local peak at the same frequency, indicating the Strouhal number corresponding to a vortex shedding of  $St = 0.266$ . This value differs from the Strouhal number of 0.2 obtained in the experiments on bluff bodies [4, 6], which could be due to an effect of a relatively high filter strength applied as the SGS model in the current simulation.

The time series and FFT results of barycenter locations are shown in Figure 11 and Figure 12. For both momentum-deficit-based and pressure-based barycenter, at all three streamwise locations, there is a local peak at  $St = 0.266$ , coinciding with the vortex shedding Strouhal number. It suggests that this high-frequency motion is related to the vortex shedding, which is also found in [5, 6]. Applying temporal filter to the time series of barycenter location, we find that there could be a potential low-frequency motion, especially pronounced in the momentum-deficit-based barycenter distribution. In [6], the existence of two distinct low frequencies was identified, one with a Strouhal number of  $St = 0.001$ , and another with even lower Strouhal number of  $St = 0.0003 - 0.0005$ . The observation of these very slow time scales requires a longer simulation time.

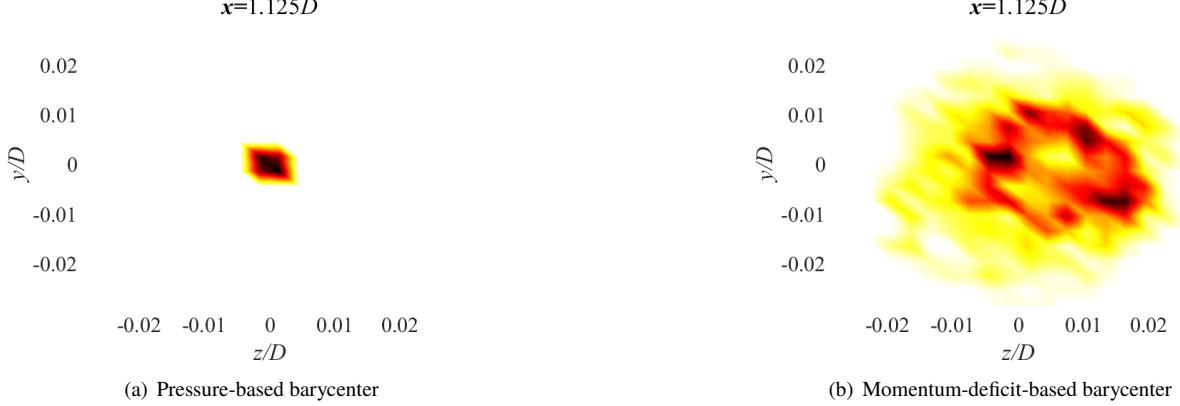


**Fig. 8 Comparison between the spread of different barycenter types at  $x = 1.125 D$ .**

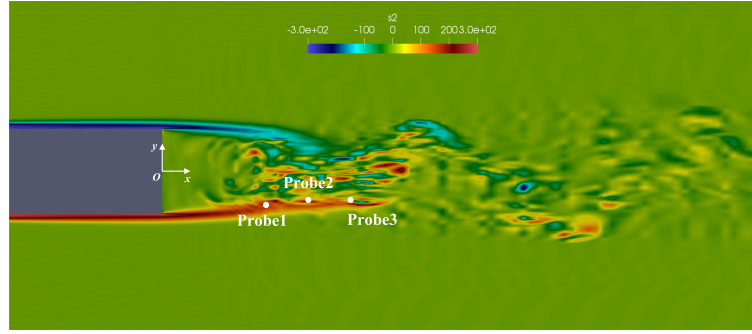


**Fig. 9 Instantaneous  $z$ -direction vorticity on the center slice in  $z$ -direction. Probe location is also shown for reference.**

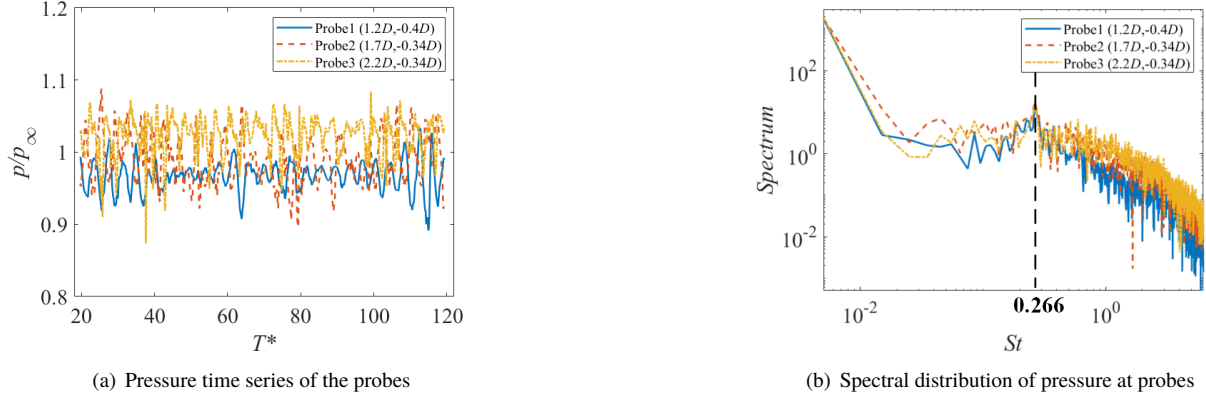


**Fig. 10 Time-dependent pressure signal and the spectra at the probes in the cylinder wake**

Instantaneous distribution of barycenter along the streamwise direction is plotted in Figure 13. Both barycenter measures show a wave-like distribution. The momentum-deficit-based barycenter has a growing amplitude and a relatively constant wave length (streamwise distance between two peaks), which is approximately  $3.4D$ . The results from three time instances separated by  $\Delta T^* = 38.56$  are shown. The pressure-based barycenter, however, has a decreasing amplitude in the far-wake area and a varying wave length along the streamwise direction. The mechanism behind the different behaviors of momentum-deficit-based barycenter and pressure-based barycenter needs further investigation.

To help understand the wake rotation, barycenter traces are drawn on  $y - z$  planes in Figure 14 and Figure 15. For

the momentum-deficit-based barycenter at  $x = 0.375D$ , the barycenter is constantly rotating at a high frequency and the axis of rotation is moving with time. Most of the trace locates at the upper portion of the domain, this highly asymmetric distribution could be related to the low-frequency motion. From  $x = 0.375D$  to  $x = 9.0D$ , the trace pattern becomes more "symmetric" with respect to the geometric centroid. For the pressure-based barycenter, it does not have a biased distribution as for the momentum-deficit-based barycenter. Although the whole trace pattern seems to be axisymmetric, the axis of rotation is not located at the geometrical centroid at all times, sometimes being substantially far from the geometrical centroid. We can also see that the pattern for the pressure-based barycenter at  $x = 9.0D$  is more chaotic than the ones from the near-wake area.

## V. Conclusions and Future Work

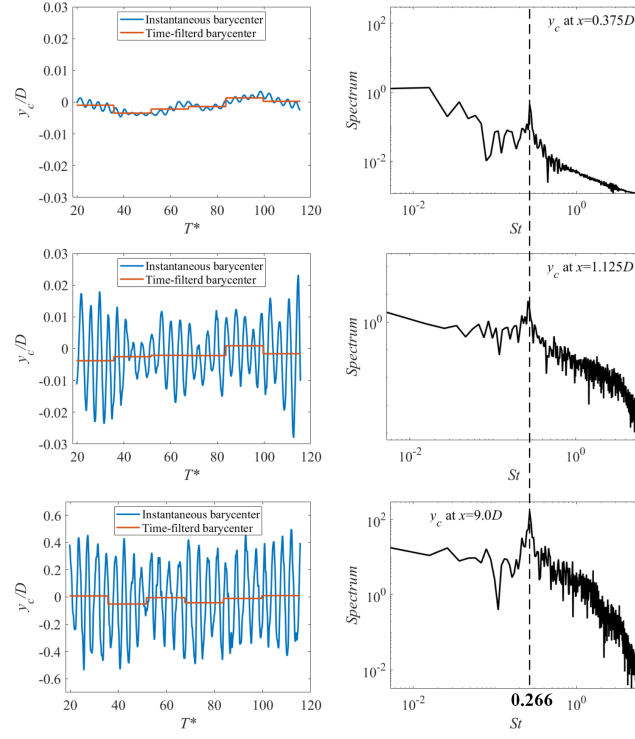
The objective of the current paper is to document the time-dependent azimuthal unsteadiness in the wake behind a body of revolution using Large-eddy Simulations. The two different definitions of the wake barycenter show similar distributions in the near-wake area but a substantially different behavior in the far-wake region. The reason behind these differences remains to be investigated. For the wake dynamics, the high-frequency motion was shown to be related to the vortex shedding. The low frequency behavior documented in the previous experimental studies [5, 6] was preliminary observed, but a longer simulation time is needed to acquire a more complete picture. Due to very large time scales associated with the low-frequency motions, and consequently, long "residence time" of coherent structures in certain azimuthal locations, the results can lead to an asymmetric distribution of the wake statistics, even in moderately long-term computational and experimental studies. In this case, exploring the ways of shifting the asymmetries in the system's behavior in computations and/or experiments would be of interest.

## Acknowledgements

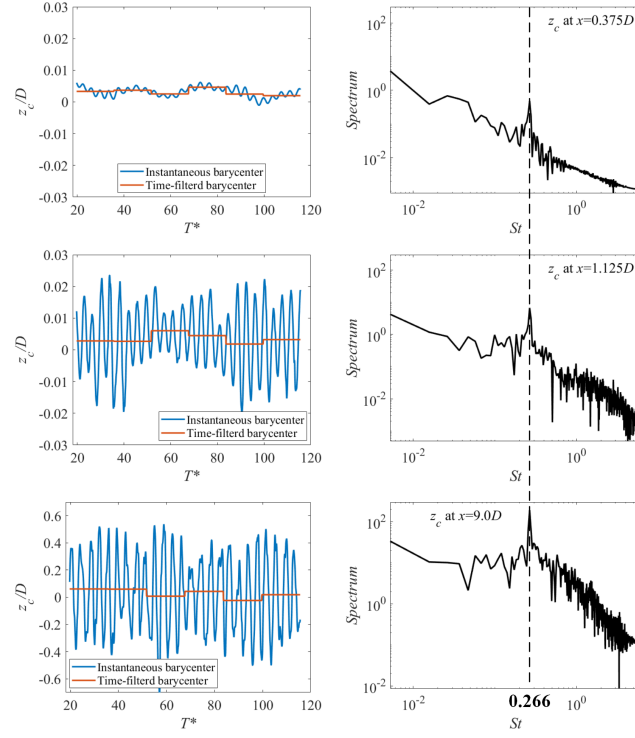
The current work is supported by NSF CBET grant # 1707075.

## References

- [1] Jiménez, J. J., Hultmark, M., and Smits, A. J., "The intermediate wake of a body of revolution at high Reynolds numbers," *J. Fluid Mech.*, Vol. 659, 2010, pp. 516–539.
- [2] Grandemange, M., Gohlke, M., Parezanović, V., and Cadot, O., "On experimental sensitivity analysis of the turbulent wake from an axisymmetric blunt trailing edge," *Phys. Fluids*, Vol. 24, 2012, p. 035106.
- [3] Ashok, A., Buren, T. V., and Smits, A. J., "Asymmetries in the wake of a submarine model in pitch," *J. Fluid Mech.*, Vol. 774, 2015, pp. 416–442.
- [4] Rigas, G., Oxlade, A., Morgans, A., and Morrison, J., "Low-dimensional dynamics of a turbulent axisymmetric wake," *J. Fluid Mech.*, Vol. 755, 2015, p. R5.
- [5] Gentile, V., Schrijer, F. F. J., van Oudheusden, B., and Scarano, F., "Low-frequency wake instability of an axisymmetric bluff body in pitch," *Proceedings of the 18th International Symposium on the Application of Laser and Imaging Techniques to Fluid Mechanics, Lisbon, Portugal*, 2016.
- [6] Gentile, V., Schrijer, F. F. J., Oudheusden, B. W. V., and Scarano, F., "Low-frequency behavior of the turbulent axisymmetric near-wake," *Phys. Fluids*, Vol. 28, 2016, p. 065102.
- [7] Seidl, V., Muzaferija, S., and Peric, M., "Parallel DNS with local grid refinement," *Appl. Sci. Res.*, Vol. 59, 1998, pp. 379–394.
- [8] Rodriguez, I., Borell, R., Lemkuhl, O., and Oliva, A., "Direct numerical simulation of the flow over a sphere at  $Re = 3700$ ," *Journal of Fluid Mechanics*, Vol. 679, 2011, pp. 263–287.
- [9] Rodriguez, I., Lemkuhl, O., Borell, R., and Oliva, A., "Flow dynamics in the turbulent wake of a sphere at sub-critical Reynolds numbers," *Comp. Fluids*, Vol. 80, 2013, pp. 233–243.
- [10] Fischer, P. F., Lottes, J. W., and Kerkemeier, S. G., "Nek5000 Web page," , 2017. [Http://nek5000.mcs.anl.gov](http://nek5000.mcs.anl.gov).
- [11] Patera, A. T., "A spectral element method for fluid dynamics: Laminar flow in a channel expansion," *J. Comp. Phys.*, Vol. 54, No. 3, 1984, pp. 468–488.

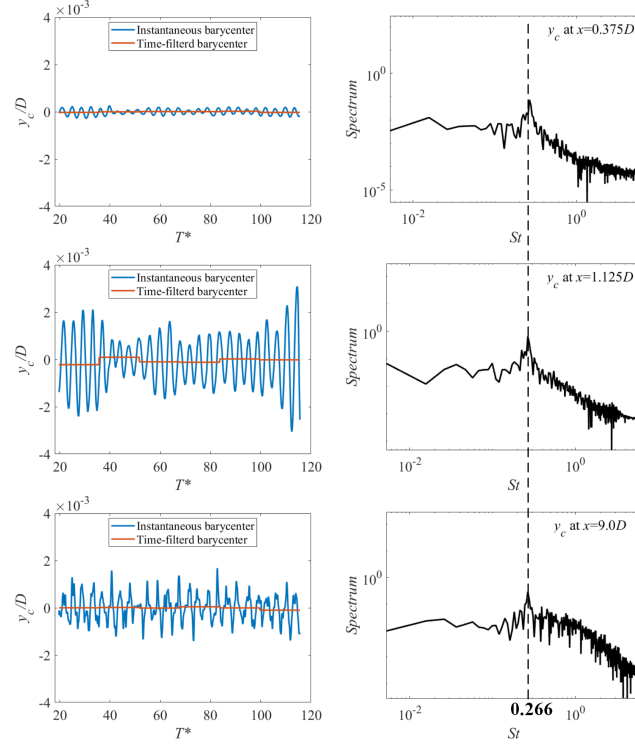


(a)  $y$  coordinate

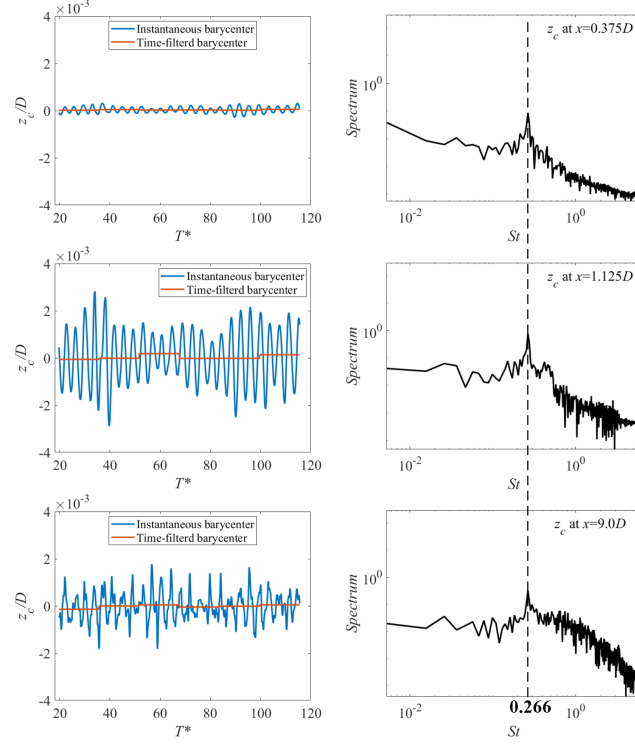


(b)  $z$  coordinate

**Fig. 11 Time series and spectral distribution of momentum-deficit-based barycenter locations.**



(a)  $y$  coordinate



(b)  $z$  coordinate

**Fig. 12** Time series and spectral distribution of pressure-based barycenter locations.

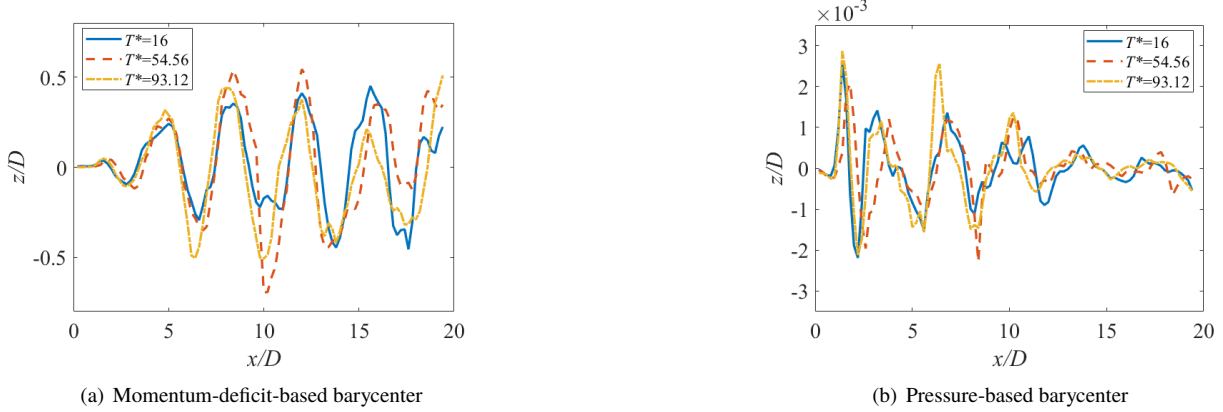


**Fig. 13 Instantaneous distribution of a barycenter location projected onto  $x - z$  plane.**

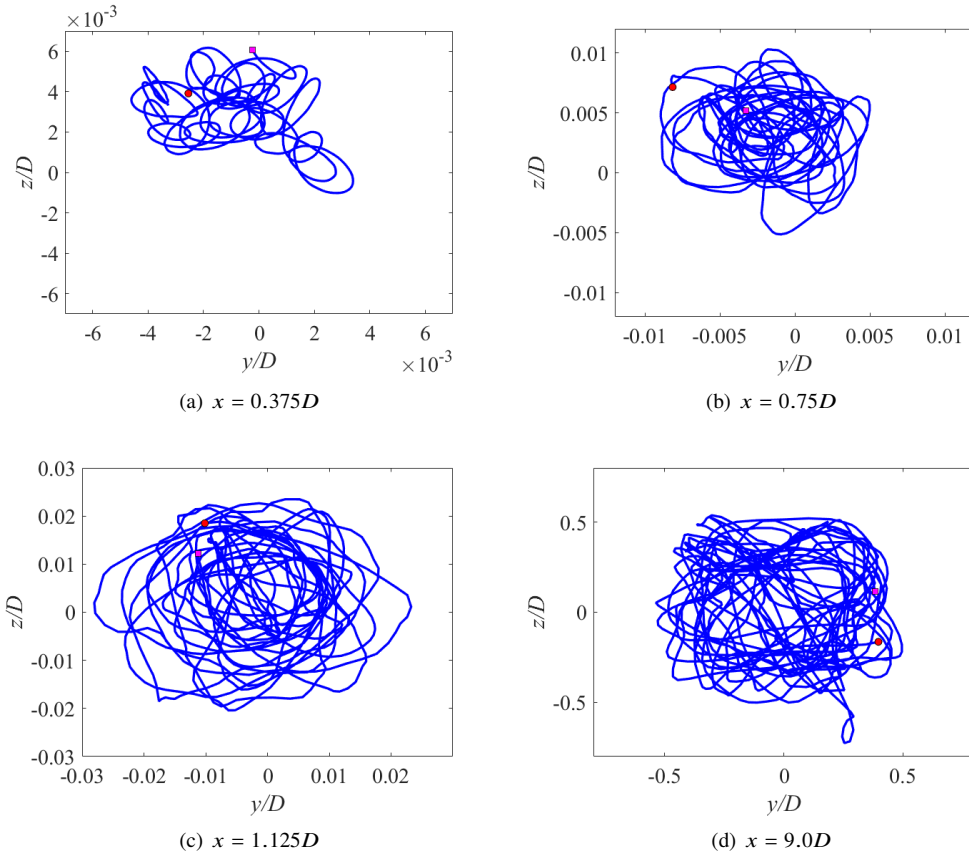


**Fig. 14 Trace of momentum-deficit-based barycenter on  $y - z$  plane collected over the non-dimensional simulation time  $T^* = 96$ . The blue solid line represents the trace of barycenter. The red circle and magenta square represent the start and end points, respectively. The range of the axes are scaled for different streamwise positions to have a clear view.**

- [12] Deville, M. O., Fischer, P. F., and Mund, E. H., *High-order methods for incompressible fluid flow*, Cambridge University Press, Cambridge, UK, 2002.
- [13] Fischer, P., “An Overlapping Schwarz Method for Spectral Element Solution of the Incompressible Navier-Stokes Equations,” *J. Comp. Phys.*, Vol. 133, 1997, pp. 84–101.

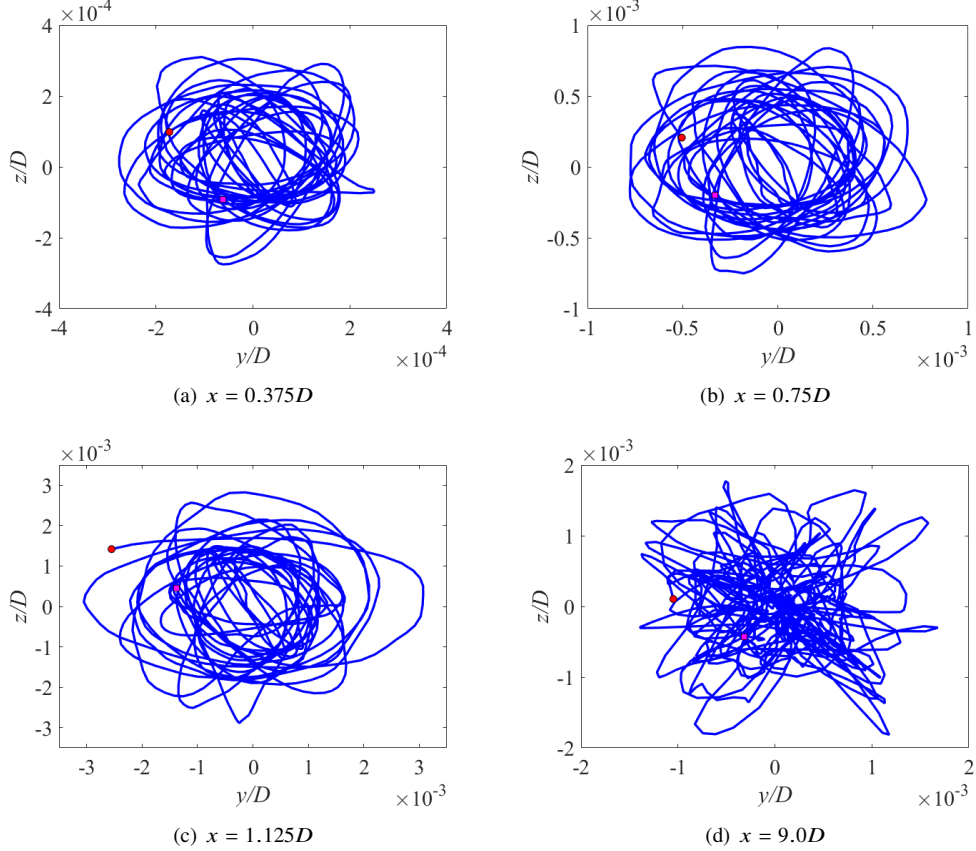


**Fig. 15 Trace of pressure-based barycenter on  $y - z$  plane collected over the non-dimensional simulation time  $T^* = 96$ . The blue solid line represents the trace of barycenter. The red circle and magenta square represent the start and end points, respectively. The range of the axes are scaled for different streamwise positions to have a clear view.**

- [14] Wang, Z. J., Fidkowski, K., Abgrall, R., Bassi, F., Caraeni, D., Cary, A., Deconinck, H., Hartmann, R., Hillewaert, K., Huynh, H., Kroll, N., May, G., Persson, P.-O., van Leer, B., and Visbal, M., “High-Order CFD Methods: Current Status and Perspective,” *Int. J. Numer. Meth. Fluids*, 2012, pp. 1–42. DOI: 10.1002/fld.
- [15] Fischer, P., Lottes, J., Pointer, D., and Siegel, A., “Petascale Algorithms for Reactor Hydrodynamics,” *Journal of Physics Conference Series*, Vol. 125, 2008, p. 012076.
- [16] Fischer, P., Pointer, D., Obabko, A., Smith, J., and Childs, H., “Simulation of Turbulent Diffusion in 217-pin Wire-Wrapped Sodium Fast Reactor Fuel Assemblies,” Tech. Rep. ANL-AFCI-267, 2009. DOE Advanced Fuel Cycle Initiative.
- [17] Kerkemeier, S., Parker, S., and Fischer, P. F., “Scalability of the Nek5000 Spectral Element Code,” Jülich Blue Gene/P Extreme Scaling Workshop, 2010. Technical report, Forschungszentrum Jülich.
- [18] Team, T. C., “The CESAR Codesign Center: Early Results,” In proceedings of the DOE exascale research conference, Portland, OR, <http://cesar.mcs.anl.gov/content/cesar-codesign-center-early-results>, 2012.
- [19] Offermans, N., Marin, O., Schanen, M., Gong, J., Fischer, P., Schlatter, P., and Merzari, E., “On the strong scaling of the spectral element solver Nek5000 on petascale systems,” *Proceedings of the Exascale Applications and Software Conference*, 2016.
- [20] Fischer, P. F., and Mullen, J. S., “Filter-based stabilization of spectral element methods,” *Comptes rendus de l'Académie des sciences, Série I- Analyse numérique*, Vol. 332, 2001, pp. 265–270.
- [21] Chatterjee, T., and Peet, Y. T., “Regularization modeling for large-eddy simulation in wall bounded turbulence: An explicit filtering-based approach,” *Int. J. Numer. Meth. Fluids*, Vol. 179, 2018, pp. 1–17. DOI: 10.1002/fld.4508.

- [22] Dong, S., Karniadakis, G. E., and Chrissostomidis, C., “A robust and accurate outflow boundary condition for incompressible flow simulations on severely-truncated unbounded domains,” *Journal of Computational Physics*, Vol. 261, 2014, pp. 83–105.
- [23] Grandemange, M., Gohlke, M., and Cadot, O., “Statistical axisymmetry of the turbulent sphere wake,” *Exp. Fluids*, Vol. 55, 2014, p. 1838.